

Two-dimensional band structure in honeycomb metal-organic frameworks

Avijit Kumar,¹ Kaustuv Banerjee,¹ Adam S. Foster,^{2,3,4} and Peter Liljeroth^{1,*}

¹*Department of Applied Physics, Aalto University School of Science,
PO Box 15100, 00076 Aalto, Finland*

²*COMP Center of Excellence, Department of Applied Physics,
Aalto University School of Science,
P.O. Box 11100, FI-00076 Aalto, Finland*

³*Division of Electrical Engineering and Computer Science,
Kanazawa University, Kanazawa 920-1192, Japan*

⁴*Institut für Physikalische Chemie, Johannes Gutenberg-Universität Mainz,
Duesbergweg 10-14, D-55099 Mainz, Germany*

arXiv:1711.01128v1 [cond-mat.mtrl-sci] 3 Nov 2017

* peter.liljeroth@aalto.fi

Metal-organic frameworks (MOFs) are an important class of materials that present intriguing opportunities in the fields of sensing, gas storage, catalysis, and optoelectronics [1–4]. Very recently, two-dimensional (2D) MOFs have been proposed as a flexible material platform for realizing exotic quantum phases including topological and anomalous quantum Hall insulators [5–11]. Experimentally, direct synthesis of 2D MOFs has been essentially confined to metal substrates [12–16, 19–21], where the interaction with the substrate masks the intrinsic electronic properties of the MOF. Here, we demonstrate synthesis of 2D honeycomb metal-organic frameworks on a weakly interacting epitaxial graphene substrate. Using low-temperature scanning tunneling microscopy (STM) and atomic force microscopy (AFM) complemented by density-functional theory (DFT) calculations, we show the formation of 2D band structure in the MOF decoupled from the substrate. These results open the experimental path towards MOF-based designer quantum materials with complex, engineered electronic structures with potential applications in devices with currently inaccessible and unforeseen functionalities [17].

The synthetic flexibility and tuneable electronic properties of MOFs stem from the choice of metal atoms, organic molecules, the linker chemistry and electronic and magnetic interactions among the building blocks [5, 8, 10, 11, 18, 19]. For example, it is possible to realize honeycomb and Kagome lattices that are expected to give rise to Dirac cones and flat bands in the band structure [5–8]. Introducing spin-orbit coupling in hexagonal MOFs should result in the opening of topologically non-trivial band gaps and the realization of organic topological insulators. Further, the immense design flexibility suggests MOFs as an ideal tuneable platform for realizing organic quantum materials with exotic electronic ground states such as quantum anomalous Hall insulators, Kitaev spin liquids, and superconductors [5–11]. However, experimental study of these phases requires synthesis methods that yield monolayer MOFs on weakly interacting substrates such that their intrinsic electronic properties can be probed.

Procedures for direct growth of 2D MOFs exist, *e.g.* through synthesis on the air-liquid interface or by chemical vapour deposition (CVD) in ultra-high vacuum (UHV) conditions [12–14, 19–21]. CVD growth is typically carried out on metallic substrates where various types of frameworks have been studied in detail [18, 19]. However, the strong hybridization

with the underlying substrate masks the intrinsic properties of the frameworks. This problem has been overcome in the case of single molecules by the use of ultrathin insulating films [22–24] and inert 2D materials such as graphene [25–28] that electronically decouple the molecule from the metallic substrate. Unfortunately, self-assembly and, in particular, on-surface chemical reactions are a virtual *terra incognita* on weakly interacting, non-catalytic substrates [28–33] and therefore the experimental observation of the intrinsic electronic properties of 2D MOFs has been elusive.

Here, we demonstrate the controlled synthesis of high quality honeycomb MOFs on epitaxial graphene using different organic linkers (dicyanobiphenyl, DCBP, and dicyanoanthracene, DCA) with cobalt metal atoms. We characterize the structures using low-temperature STM and AFM. We demonstrate the formation of 2D band structure in the DCA-Co MOF by scanning tunneling spectroscopy (STS) measurements complemented by DFT calculations.

Figure 1 shows the structure of the honeycomb MOFs - DCBP_3Co_2 and DCA_3Co_2 - synthesized on epitaxial graphene grown on Ir(111) (G/Ir(111)) surface. Figure 1a shows an overview STM topography image of DCBP_3Co_2 MOF possessing a long-range ordered honeycomb structure. An atomically resolved non-contact AFM (nc-AFM) image of DCBP_3Co_2 MOF using a CO-terminated tip is shown in Fig. 1b. The hexagonal symmetry and non-planarity of DCBP molecules (finite torsional angle between two phenyl rings along the long axis) making the framework chiral are readily apparent. This is consistent with the DFT calculated structure on graphene (Fig. 1c) and simulated nc-AFM image as shown in Supplementary Information (SI) Fig. S1. The calculated gas-phase structure shows that the cobalt atom is in the plane of the framework while it relaxes slightly (about 10 pm) towards the surface on graphene.

Similar to the DCBP_3Co_2 , DCA_3Co_2 MOF also reveals a symmetric honeycomb structure as shown by the STM topography image in Fig. 1d. A typical STM image of a large area DCA_3Co_2 MOF is shown in SI Fig. S2 where various domains of different sizes are clearly visible. Compared to DCBP_3Co_2 , the domains of the DCA_3Co_2 MOF are smaller in size probably due to the more limited mobility of DCA on the graphene surface. A DFT simulated structure corresponding to DCA_3Co_2 framework is shown in Fig. 1e. Here also the DCA molecules and cobalt lie in the plane of the framework for gas-phase optimized structures (see SI for the computational details). In both MOFs, we estimate the N-Co

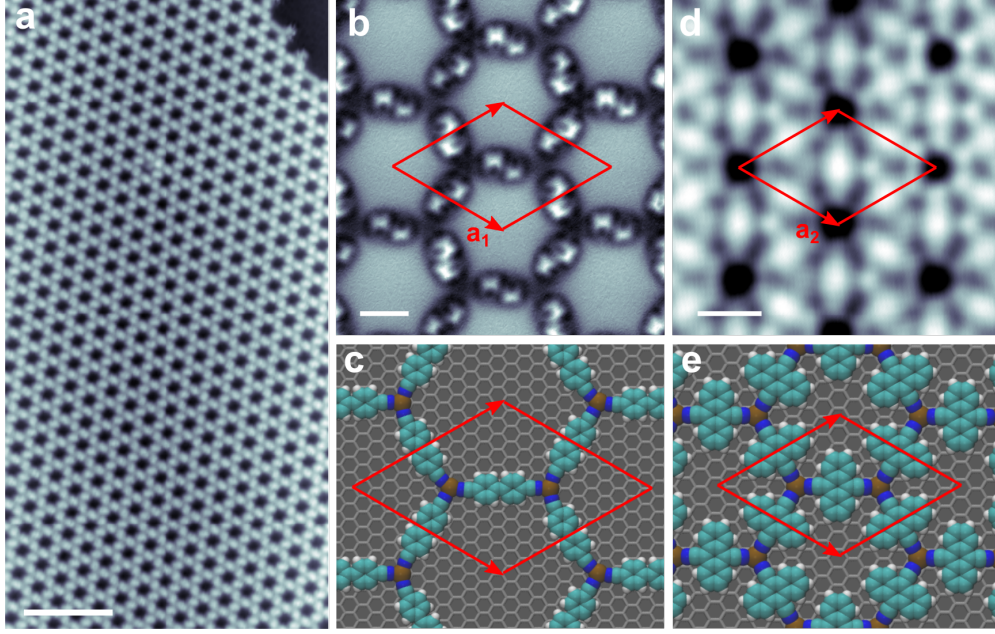


FIG. 1. **Overview of two MOFs.** **a**, An STM overview image of a honeycomb DCBP₃Co₂ MOF on G/Ir(111) surface. Scale bar is 10 nm, imaging parameters: 1.23 V and 3.3 pA. **b**, Constant height frequency-shift (Δf) nc-AFM image of DCBP₃Co₂ MOF acquired with a CO-terminated tip. Scale bar is 1 nm. **c**, DFT simulated structure of DCBP₃Co₂ MOF on graphene. **d**, STM topography image of DCA₃Co₂ MOF. The scale bar is 1 nm, imaging parameters: -1 V, 15 pA. **e**, DFT simulated structure of DCA₃Co₂ MOF on graphene. Red parallelogram indicates the unit cell.

coordination bond length from the high resolution STM images to be $1.55 \pm 0.5 \text{ \AA}$ (see SI Fig. S3) which is comparable to the value extracted from DFT relaxed structures and earlier reports [12]. Further, the measured lattice constant of the DCBP₃Co₂ MOF, \mathbf{a}_1 is $27.9 \pm 0.4 \text{ \AA}$ while DCA₃Co₂ MOF possesses a lattice constant \mathbf{a}_2 of $19.6 \pm 0.2 \text{ \AA}$ (compared to the 27.3 \AA and 20.0 \AA as extracted from our DFT optimized structure, respectively).

We synthesize the MOFs by first depositing the organic molecules, followed by deposition of the metal atoms with subsequent annealing. Each of the honeycomb MOFs is separately preceded by the formation of an assembly of single complexes upon deposition of Co atoms on the molecular-layer on G/Ir(111) surface. The network of these complexes is stabilized through intermolecular hydrogen bonds between the cyano and phenyl groups. While DCBP forms four-fold mononuclear single complexes (DCBP₄Co) and a stripe of four-fold framework (DCBP₃Co) depending on the DCBP:Co stoichiometry, DCA forms only mononuclear

three-fold (DCA_3Co) complexes which is unambiguously confirmed by nc-AFM image (see SI Figs. S4 and S5). We attribute the absence of four-fold DCA_4Co to a larger steric hindrance compared to that of a four-fold structure of DCBP_4Co .

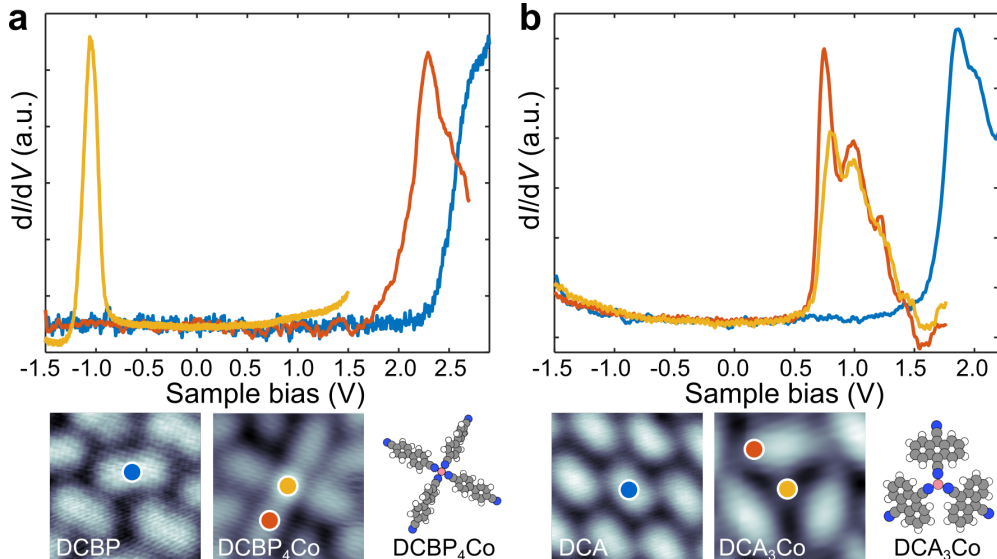


FIG. 2. **STS on single complexes.** **a**, dI/dV spectra measured on a single DCBP molecule (blue curve), and the Co atom (orange) and on the ligand (red) of a DCBP_4Co complex. **b**, dI/dV spectra measured on a single DCA molecule (blue curve), and the cobalt atoms (orange) and the ligand (red) on a single DCA_3Co complex. The positions of the spectra are shown on the bottom panels.

Figure 2 compares dI/dV spectra recorded on single molecules and the corresponding single metal-organic complexes. As shown in Fig. 2a, dI/dV spectrum recorded on a DCBP molecule shows a shoulder at 2.7 V corresponding to the lowest unoccupied molecular orbital (LUMO) (see SI Fig. S5). The peak due to the highest occupied molecular orbital (HOMO) of the molecule is not visible within the recorded bias range of the spectrum. On a single DCBP_4Co complex, dI/dV reveals two peaks at 2.3 V and -1 V with corresponding electronic states located on DCBP and Co center, respectively. Based on the bias-dependent STM imaging of the four-fold phases and dI/dV spectroscopy of DCBP molecule as a function of distance from Co center (see SI Figs. S5 and S6), it is clear that the peak 2.3 V originates from the LUMO of the DCBP molecule. The shift of the molecular LUMO towards the Fermi level by 0.4 V indicates that there is an electrostatic shift of the orbital energy due to the Co atom of the complex and other complexes present in the vicinity.

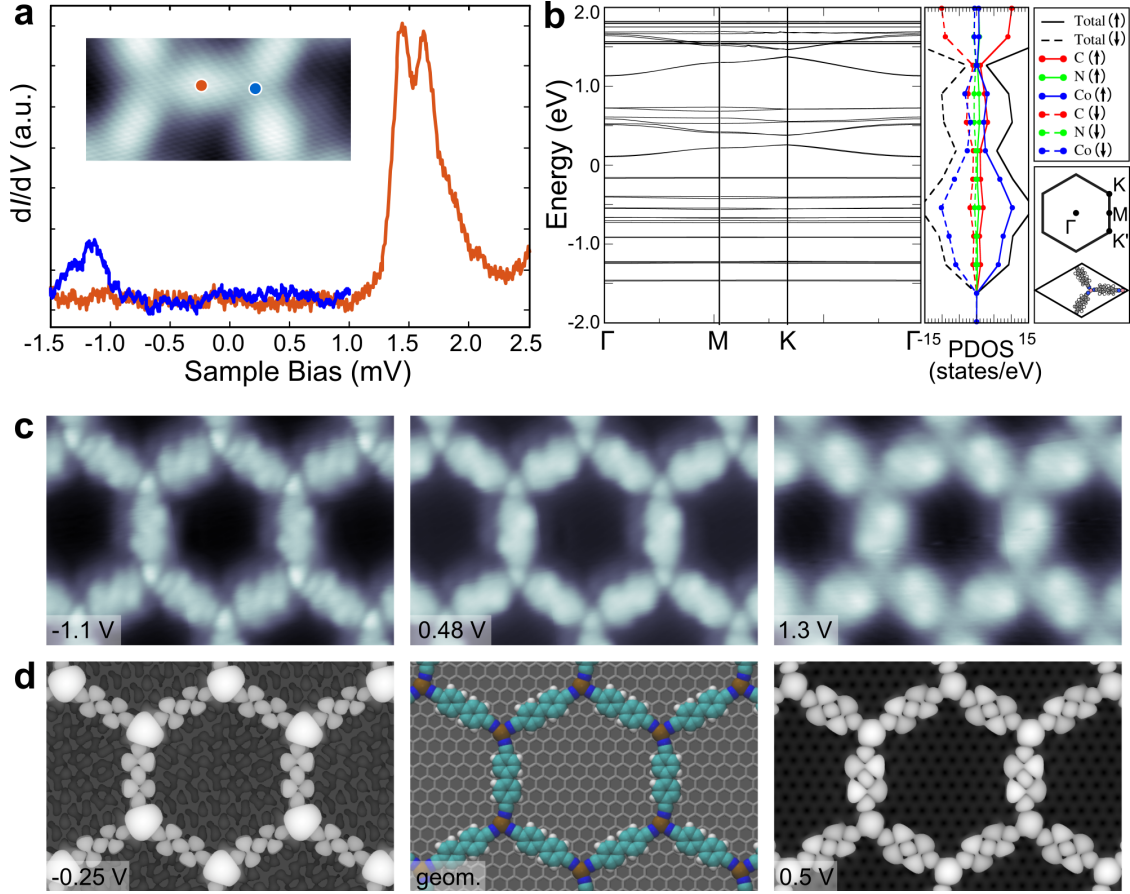


FIG. 3. **Electronic properties of honeycomb DCBP₃Co₂ MOF.** **a**, STS recorded on honeycomb DCBP₃Co₂ at the positions shown in the inset. **b**, Calculated band structure and total PDOS of DCBP₃Co₂ MOF. **c,d** Experimental (panel c) and simulated STM images (panel d) at the energies indicated in the figure. Scan size is $6.2 \times 4 \text{ nm}^2$.

dI/dV spectra on single DCA molecule on G/Ir(111) also reveals a peak at 1.8 V as shown in Fig 2b. The gating effect due to Co atoms is also observed in the DCA₃Co single complexes. The dI/dV spectra recorded on DCA of the complex shows that the LUMO shifts down to 750 mV and three satellite vibronic peaks also become visible. The vibronic mode energy of ~ 200 mV fits well with the expected energy of the C-C vibration [34, 35]. The assignment of the peak to the molecular LUMO is also evident from the STM images (see SI Figs. S4 and S7). dI/dV spectra recorded on Co center of the complex shows an additional shoulder at the onset of the peak. We attribute this shoulder to the metal-state as the metal center becomes brighter in the STM images at sample bias beyond 0.7 V (see SI Fig. S4).

Figure 3a shows dI/dV spectra recorded on DCBP molecule in the DCBP_3Co_2 MOF has a peak at 1.44 V which we ascribe to the elastic LUMO peak with corresponding vibronic replica at 1.62 V. The small line-width of molecular LUMO and the observation of satellite vibronic peaks indicates that the intermolecular electronic coupling in the framework is weak such that we have isolated molecular electronic states. The spectrum recorded on the Co center reveals a faint peak at -1150 mV, which is visible in the background corrected spectrum (see SI Fig. S8). The state is localized only at the metal-center.

We have used DFT to calculate the band structure of the DCBP_3Co_2 MOF as shown in Fig. 3b for the antiferromagnetic ground state. While DFT underestimates the band gap, it correctly captures the nature of the lowest lying bands: the occupied states have a stronger metal character compared to the unoccupied states, which are mostly composed of the ligand states (Fig. 3c,d). The enhanced contrast on the metal atoms and ligands can be seen at negative and positive bias, respectively, compared to the STM topography in the gap (Figs. 3c middle panel). However, DFT seems to overestimate the band-width of the unoccupied ligand-derived states compared to the experiment. This could be related to how well the torsional angle between the phenyl rings of DCBP molecule is estimated by DFT as this is known to control the $\pi - \pi$ conjugation within the backbone of the molecule [36]. The coupling is enhanced for the planar, smaller DCA linker as demonstrated below.

A substantial in-plane electronic hybridization and formation of energy bands with significant width in DCA_3Co_2 MOF is evidenced by dI/dV spectroscopy, dI/dV maps and DFT calculations. dI/dV spectrum (Fig. 4, blue) recorded at the center of the ring (constituting six DCA lobes) has three peaks at 260, 480, and 860 mV. Considering the separation between the first and the second peak, ~ 220 mV, the second peak could still be interpreted as a vibronic satellite. However, the separation between the second and the third peak rules out vibronic origin. The spectrum at the center of DCA molecule (red curve) shows that the first peak shifts to 360 mV, while that on cobalt (cyan curve) has the first peak at 320 mV. The systematic evolution of the spectra across the framework is shown in the SI Fig. S9. Comparison of the spectra at the lobe and center of DCA and cobalt in the DCA_3Co_2 MOF to that of DCA_3Co single complex indicates that there is additional intensity in the MOF at energies higher than 700 mV (see SI Fig. S10). As the dI/dV signal is directly proportional to the local density of states (LDOS), this is direct evidence of additional electronic states. Further, we have recorded dI/dV maps of the same area at different energies as shown in

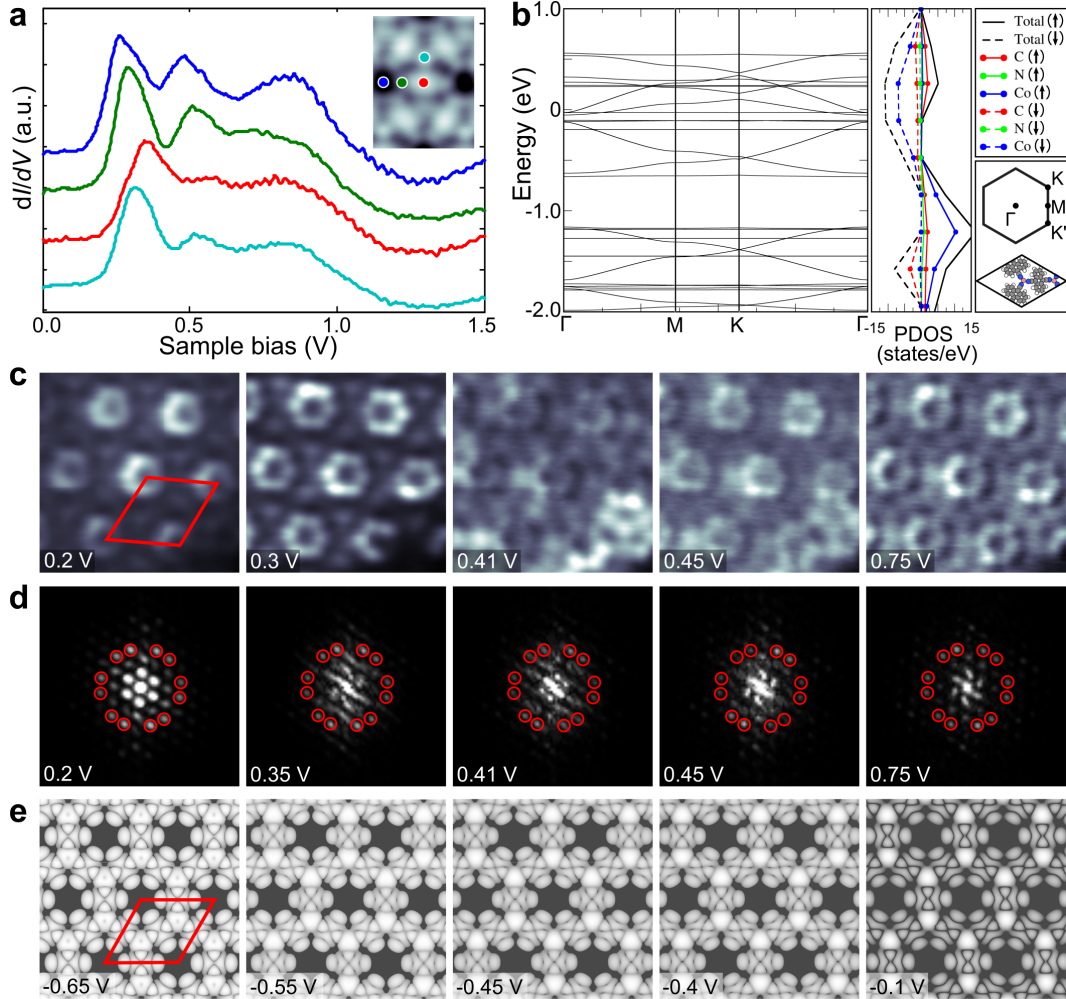


FIG. 4. **Electronic properties of honeycomb DCA_3Co_2 MOF.** **a**, STS recorded on honeycomb DCA_3Co_2 MOF on the positions indicated in the inset. **b**, Calculated band structure and total PDOS of DCA_3Co_2 MOF. **c**, **d**, **e**, Experimentally recorded constant-height dI/dV (panel c scan size $4.7 \times 4.7 \text{ nm}^2$), FFTs of large area dI/dV maps (panel d), and simulated LDOS (panel e) at the energies indicated in the panels. The unit cell is indicated by the red parallelogram in panels c and e

Fig 4c. At lower energies, 200-300 mV, DCA molecules feature LUMO lobes and Co appears to be bright while at higher energies, e.g. 750 mV, metal states have lower intensity. At intermediate energies, 410 and 450 mV, there exists extra features in the dI/dV maps superimposed on the existing framework. To understand these features, we have taken Fourier transforms (FFT) of a large area dI/dV maps (Fig. 4d). Apart from the 12 outer spots (red circles) corresponding to the honeycomb structure of DCA_3Co_2 MOF, there exists in-

ternal structure which evolves continuously with the bias. The spots in this quasi-particle interference pattern correspond to scattering vectors connecting the initial and final states of the scattering process at the given energy. In addition to this joint density-of-states, they contain information on the nature of the allowed scattering processes [37–39]. While quantitative analysis of the experimental patterns is difficult due to the other overlapping peaks stemming from the geometry as well as the limited sample size (number of repetitive unit cells), they indicate the formation of an extended electron system with considerable dispersion (band width).

The calculated electronic band structure using DFT for the symmetric, ferromagnetic DCA_3Co_2 framework without graphene is shown in Fig. 4b. In line with the calculations done for DCA_3Cu_2 and DCA_3Mn_2 MOFs [7, 9], the band structure of DCA_3Co_2 MOF has a number of flat-bands and Dirac cones. While the antiferromagnetic structure is slightly lower in energy (by 0.05 eV), the ferromagnetic state better reproduces the experimental results and we concentrate on it here (see SI Fig. S11). The presence of a large gap between -0.7 eV and -1.2 eV in the calculated band structure and lack of states below the Fermi energy in the dI/dV spectra until -1.5 V suggests that the energy corresponding to the experimental Fermi level lies below the flat band at energy -0.7 V. The DFT calculation suggests that the bottom of the conduction band consists of a flat band and a Dirac cone stemming from the DCA states and the Kagome symmetry of the lattice. Subsequently, at higher energies, there are also relatively flat bands originating mostly from the metal atom orbitals and band with more mixed character. This overall picture is consistent with the experiments where we first see intensity on the molecules with metal states emerging at higher energies and an overall band width of ~ 1 eV.

In summary, we have demonstrated synthesis of long range, ordered domains of two honeycomb MOFs on epitaxial graphene surface. While DCBP_3Co_2 -MOF only has weak coupling between the building blocks, DCA_3Co_2 -MOF shows significant in-plane hybridization resulting in the formation of 2D electronic states with significant band width. These observations point towards the experimental realization of engineered 2D-MOFs with exotic electronic properties.

ACKNOWLEDGEMENTS

This research made use of the Aalto Nanomicroscopy Center (Aalto NMC) facilities and was supported by the European Research Council (ERC-2011-StG No. 278698 "PRECISE-NANO") and the Academy of Finland (Projects no. 305635 and 311012, and Centres of Excellence Program projects no. 284594 and 284621).

AUTHOR CONTRIBUTIONS

A.K., K.B. and P.L. conceived and planned the experiment. A.K. and K.B. performed the measurements and analysed the data. A.S.F. carried out the DFT calculations. A.K. and P.L. wrote the manuscript and all authors jointly authored, commented, and corrected the manuscript.

-
- [1] C. H. Hendon, A. J. Rieth, M. D. Korzyński, and M. Dincă, "Grand challenges and future opportunities for metal-organic frameworks," *ACS Cent. Sci.* **3**, 554–563 (2017).
 - [2] L. E. Kreno, K. Leong, O. K. Farha, M. Allendorf, R. P. Van Duyne, and J. T. Hupp, "Metal-organic framework materials as chemical sensors," *Chem. Rev.* **112**, 1105–1125 (2012).
 - [3] L. Zhu, X.-Q. Liu, H.-L. Jiang, and L.-B. Sun, "Metal-organic frameworks for heterogeneous basic catalysis," *Chem. Rev.* **117**, 8129–8176 (2017).
 - [4] V. Stavila, A. A. Talin, and M. D. Allendorf, "MOF-based electronic and opto-electronic devices," *Chem. Soc. Rev.* **43**, 5994–6010 (2014).
 - [5] Z. F. Wang, N. Su, and F. Liu, "Prediction of a two-dimensional organic topological insulator," *Nano Lett.* **13**, 2842–2845 (2013).
 - [6] Z. F. Wang, Zheng Liu, and Feng Liu, "Organic topological insulators in organometallic lattices," *Nat. Commun.* **4**, 1471 (2013).
 - [7] L. Z. Zhang, Z. F. Wang, B. Huang, B. Cui, Zhiming Wang, S. X. Du, H.-J. Gao, and Feng Liu, "Intrinsic two-dimensional organic topological insulators in metal-dicyanoanthracene lattices," *Nano Lett.* **16**, 2072–2075 (2016).
 - [8] L. Dong, Y. Kim, D. Er, A. M. Rappe, and V. B. Shenoy, "Two-dimensional π -conjugated covalent-organic frameworks as quantum anomalous Hall topological insulators," *Phys. Rev.*

- Lett. **116**, 096601 (2016).
- [9] Y.-P. Wang, W.-X. Ji, C.-W. Zhang, P. Li, P.-J. Wang, B. Kong, S.-S. Li, S.-S. Yan, and K. Liang, “Discovery of intrinsic quantum anomalous Hall effect in organic Mn-DCA lattice,” *Appl. Phys. Lett.* **110**, 233107 (2017).
- [10] X. Zhang, Y. Zhou, B. Cui, M. Zhao, and F. Liu, “Theoretical discovery of a superconducting two-dimensional metal-organic framework,” *Nano Lett.* **17**, 6166–6170 (2017).
- [11] M. G. Yamada, V. Dwivedi, and M. Hermanns, “Crystalline Kitaev spin liquids,” *Phys. Rev. B* **96**, 155107 (2017).
- [12] U. Schlickum, R. Decker, F. Klappenberger, G. Zoppellaro, S. Klyatskaya, M. Ruben, I. Silanes, A. Arnau, K. Kern, H. Brune, and J. V. Barth, “Metal-organic honeycomb nanomeshes with tunable cavity size,” *Nano Lett.* **7**, 3813–3817 (2007).
- [13] G. Pawin, K. L. Wong, D. Kim, D. Sun, L. Bartels, S. Hong, T. S. Rahman, R. Carp, and M. Marsella, “A surface coordination network based on substrate-derived metal adatoms with local charge excess,” *Angew. Chem. Int. Ed.* **47**, 8442–8445 (2008).
- [14] T. Kambe, R. Sakamoto, K. Hoshiko, K. Takada, M. Miyachi, J.-H. Ryu, S. Sasaki, J. Kim, K. Nakazato, M. Takata, and H. Nishihara, “ π -conjugated nickel bis(dithiolene) complex nanosheet,” *J. Am. Chem. Soc.* **135**, 2462–2465 (2013).
- [15] J. I. Urgel, M. Schwarz, M. Garnica, D. Stassen, D. Bonifazi, D. Eciija, J. v. Barth, and W. Auwärter, “Controlling coordination reactions and assembly on a Cu(111) supported boron nitride monolayer,” *J. Am. Chem. Soc.* **137**, 2420–2423 (2015).
- [16] J. I. Urgel, D. Eciija, G. Lyu, R. Zhang, C.-A. Palma, W. Auwärter, N. Lin, and J. V. Barth, “Quasicrystallinity expressed in two-dimensional coordination networks,” *Nat. Chem.* **8**, 657–662 (2016).
- [17] D. N. Basov, R. D. Averitt, and D. Hsieh, “Towards properties on demand in quantum materials,” *Nat. Mater.* **16**, 1077 (2017).
- [18] J. V. Barth, “Molecular architectonic on metal surfaces,” *Annu. Rev. Phys. Chem.* **58**, 375–407 (2007).
- [19] L. Dong, Z. A. Gao, and N. Lin, “Self-assembly of metal-organic coordination structures on surfaces,” *Prog. Surf. Sci.* **91**, 101–135 (2016).
- [20] S. Stepanow, N. Lin, D. Payer, U. Schlickum, F. Klappenberger, G. Zoppellaro, M. Ruben, H. Brune, J.V. Barth, and K. Kern, “Surface-assisted assembly of 2D metalorganic networks

- that exhibit unusual threefold coordination symmetry,” *Angew. Chem. Int. Ed.* **46**, 710–713 (2007).
- [21] R. Sakamoto, K. Takada, T. Pal, H. Maeda, T. Kambe, and H. Nishihara, “Coordination nanosheets (CONASHs): strategies, structures and functions,” *Chem. Commun.* **53**, 5781–5801 (2017).
- [22] X. H. Qiu, G. V. Nazin, and W. Ho, “Vibrationally resolved fluorescence excited with sub-molecular precision,” *Science* **299**, 542–546 (2003).
- [23] J. Repp, G. Meyer, S. M. Stojković, A. Gourdon, and C. Joachim, “Molecules on insulating films: Scanning-tunneling microscopy imaging of individual molecular orbitals,” *Phys. Rev. Lett.* **94**, 026803 (2005).
- [24] I. Swart, L. Gross, and P. Liljeroth, “Single-molecule chemistry and physics explored by low-temperature scanning probe microscopy,” *Chem. Commun.* **47**, 9011–9023 (2011).
- [25] P. Järvinen, S. K. Hämäläinen, K. Banerjee, P. Häkkinen, M. Ijäs, Ari H., and P. Liljeroth, “Molecular self-assembly on graphene on SiO₂ and h-BN substrates,” *Nano Lett.* **13**, 3199–3204 (2013).
- [26] P. Järvinen, S. K. Hämäläinen, M. Ijäs, A. Harju, and P. Liljeroth, “Self-assembly and orbital imaging of metal phthalocyanines on a graphene model surface,” *J. Phys. Chem. C* **118**, 13320–13325 (2014).
- [27] A. Riss, S. Wickenburg, L. Z. Tan, H.-Z. Tsai, Y. Kim, J. Lu, A. J. Bradley, M. M. Ugeda, K. L. Meaker, K. Watanabe, T. Taniguchi, A. Zettl, F. R. Fischer, S. G. Louie, and M. F. Crommie, “Imaging and tuning molecular levels at the surface of a gated graphene device,” *ACS Nano* **8**, 5395–5401 (2014).
- [28] A. Kumar, K. Banerjee, and P. Liljeroth, “Molecular assembly on two-dimensional materials,” *Nanotechnology* **28**, 082001 (2017).
- [29] M. Abel, S. Clair, O. Ourdjini, M. Mossoyan, and L. Porte, “Single layer of polymeric Fe-phthalocyanine: An organometallic sheet on metal and thin insulating film,” *J. Am. Chem. Soc.* **133**, 1203–1205 (2011).
- [30] T. Dienel, J. Gómez-Díaz, A. P. Seitsonen, R. Widmer, M. Iannuzzi, K. Radican, H. Sachdev, K. Müllen, J. Hutter, and O. Gröning, “Dehalogenation and coupling of a polycyclic hydrocarbon on an atomically thin insulator,” *ACS Nano* **8**, 6571–6579 (2014).

- [31] C. Morchutt, J. Björk, S. Krotzky, R. Gutzler, and K. Kern, “Covalent coupling via dehalogenation on Ni(111) supported boron nitride and graphene,” *Chem. Commun.* **51**, 2440–2443 (2015).
- [32] C. Guo, Y. Wang, M. Kittelmann, L. Kantorovitch, A. Kühnle, and A. Floris, “Mechanisms of covalent dimerization on a bulk insulating surface,” *J. Phys. Chem. C* **121**, 10053–10062 (2017).
- [33] L. Schüller, V. Haapasilta, S. Kuhn, H. Pinto, R. Bechstein, A. S. Foster, and A. Kühnle, “Deposition order controls the first stages of a metal-organic coordination network on an insulator surface,” *J. Phys. Chem. C* **120**, 14730–14735 (2016).
- [34] J. Repp, P. Liljeroth, and G. Meyer, “Coherent electron-nuclear coupling in oligothiophene molecular wires,” *Nat. Phys.* **6**, 975–979 (2010).
- [35] J. van der Lit, M. P. Boneschanscher, D. Vanmaekelbergh, M. Ijäs, A. Uppstu, M. Ervasti, A. Harju, P. Liljeroth, and I. Swart, “Suppression of electronvibron coupling in graphene nanoribbons contacted via a single atom,” *Nat. Commun.* **4**, 2023 (2013).
- [36] L. Venkataraman, J. E. Klare, C. Nuckolls, M. S. Hybertsen, and M. L. Steigerwald, “Dependence of single-molecule junction conductance on molecular conformation,” *Nature* **442**, 904–907 (2006).
- [37] L. Petersen, P. Hofmann, E. W. Plummer, and F. Besenbacher, “Fourier transform-STM: determining the surface Fermi contour,” *J. Electron. Spectrosc. Relat. Phenom.* **109**, 97–115 (2000).
- [38] J. E. Hoffman, E. W. Hudson, K. M. Lang, V. Madhavan, H. Eisaki, S. Uchida, and J. C. Davis, “A four unit cell periodic pattern of quasi-particle states surrounding vortex cores in $\text{Bi}_2\text{Sr}_2\text{CaCu}_2\text{O}_{8+\delta}$,” *Science* **295**, 466–469 (2002).
- [39] P. Roushan, J. Seo, C. V. Parker, Y. S. Hor, D. Hsieh, D. Qian, A. Richardella, M. Z. Hasan, R. J. Cava, and A. Yazdani, “Topological surface states protected from backscattering by chiral spin texture,” *Nature* **460**, 1106 (2009).
- [40] L. Bartels, G. Meyer, and K.-H. Rieder, “Controlled vertical manipulation of single CO molecules with the scanning tunneling microscope: A route to chemical contrast,” *Appl. Phys. Lett.* **71**, 213 (1997).
- [41] L. Gross, F. Mohn, N. Moll, P. Liljeroth, and G. Meyer, “The chemical structure of a molecule resolved by atomic force microscopy,” *Science* **325**, 1110–1114 (2009).

- [42] I. Horcas, R. Fernández, J. M. Gómez-Rodríguez, J. Colchero, J. Gómez-Herrero, and A. M. Baro, “WSXM: A software for scanning probe microscopy and a tool for nanotechnology,” *Rev. Sci. Instrum.* **78**, 013705 (2007).
- [43] <http://gwyddion.net/>.
- [44] D. Nečas and P. Klapetek, “Gwyddion: an open-source software for SPM data analysis,” *Cent. Eur. J. Phys.* **10**, 181–188 (2012).
- [45] G. Kresse and J. Furthmüller, “Efficiency of ab-initio total energy calculations for metals and semiconductors using a plane-wave basis set,” *Comp. Mat. Sci.* **6**, 15 (1996).
- [46] G. Kresse and J. Furthmüller, “Efficient iterative schemes for ab initio total-energy calculations using a plane-wave basis set,” *Phys. Rev. B* **54**, 11169 (1996).
- [47] J. Klimeš, D. R. Bowler, and A. Michaelides, “Chemical accuracy for the van der Waals density functional,” *J. Phys. Condens. Matter* **22**, 022201 (2010).
- [48] J. Klimeš, D. R. Bowler, and A. Michaelides, “Van der Waals density functionals applied to solids,” *Phys. Rev. B* **83**, 195131 (2011).
- [49] T. Björkman, A. Gulans, A. Krashennnikov, and R. M. Nieminen, “van der Waals bonding in layered compounds from advanced density-functional first-principles calculations,” *Phys. Rev. Lett.* **108**, 235502 (2012).
- [50] P. E. Blöchl, “Projector augmented-wave method,” *Phys. Rev. B* **50**, 17953 (1994).
- [51] D. E. P. Vanpoucke and G. Brocks, “Formation of Pt-induced Ge atomic nanowires on Pt/Ge(001): A density functional theory study,” *Phys. Rev. B* **77**, 241308 (2008).
- [52] Prokop Hapala, Ruslan Temirov, F Stefan Tautz, and Pavel Jelinek, “Origin of High-Resolution IETS-STM Images of Organic Molecules with Functionalized Tips,” *Phys. Rev. Lett.* **113**, 226101 (2014).
- [53] <https://github.com/SINGROUP>.
- [54] B. R. Brooks, C. L. Brooks III, A. D. Mackerell Jr., L. Nilsson, R. J. Petrella, B. Roux, Y. Won, G. Archontis, C. Bartels, S. Boresch, A. Caffisch, L. Caves, Q. Cui, A. R. Dinner, M. Feig, S. Fischer, J. Gao, M. Hodosek, W. Im, K. Kuczera, T. Lazaridis, J. Ma, V. Ovchinnikov, E. Paci, R. W. Pastor, C. B. Post, J. Z. Pu, M. Schaefer, B. Tidor, R. M. Venable, H. L. Woodcock, X. Wu, W. Yang, D. M. York, and M. Karplus, “CHARMM: The biomolecular simulation program,” *J. Comput. Chem.* **30**, 1545–1614 (2009).

- [55] P. Hapala, G. Kichin, C. Wagner, F. S. Tautz, R. Temirov, and P. Jelinek, “Mechanism of high-resolution STM/AFM imaging with functionalized tips,” *Phys. Rev. B* **90**, 085421 (2014).
- [56] J. Welker, E. Illek, and F. J. Giessibl, “Analysis of force-deconvolution methods in frequency-modulation atomic force microscopy,” *Beilstein J. Nanotechnol.* **3**, 238–248 (2012).

SUPPLEMENTARY INFORMATION

Simulated nc-AFM image of DCBP₃Co₂ MOF

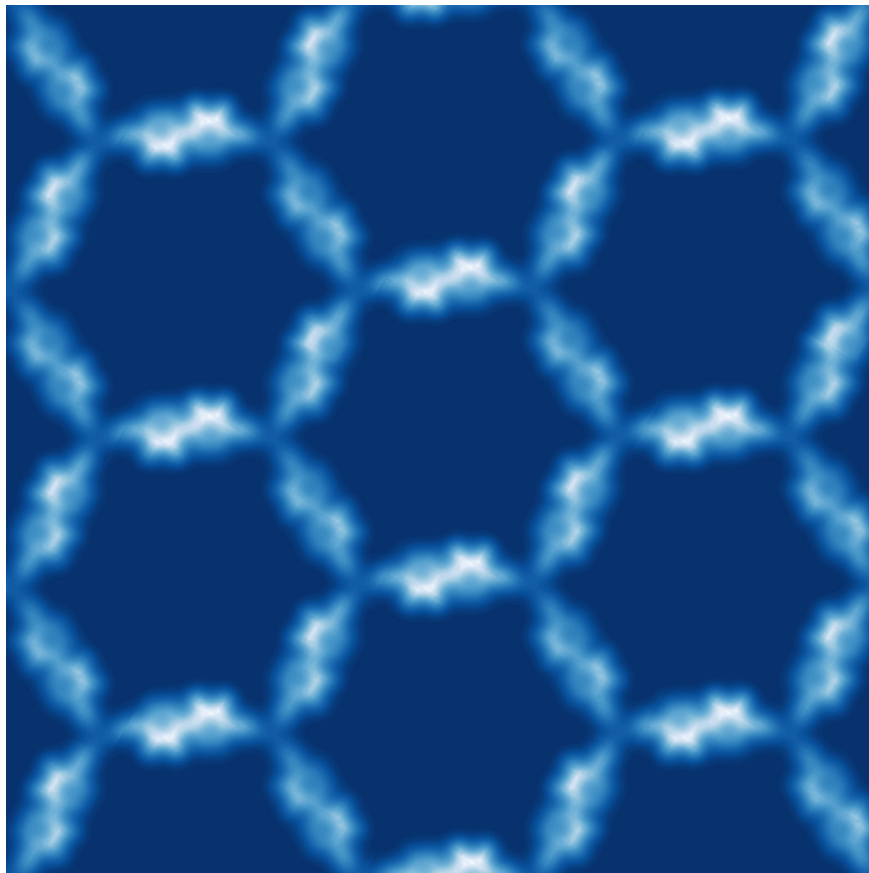


FIG. S1. Simulated nc-AFM image of DFT optimized DCBP₃Co₂ MOF shows non-planarity of DCBP molecules and the chirality exhibited by the framework.

Large area image of DCA_3Co_2 MOF

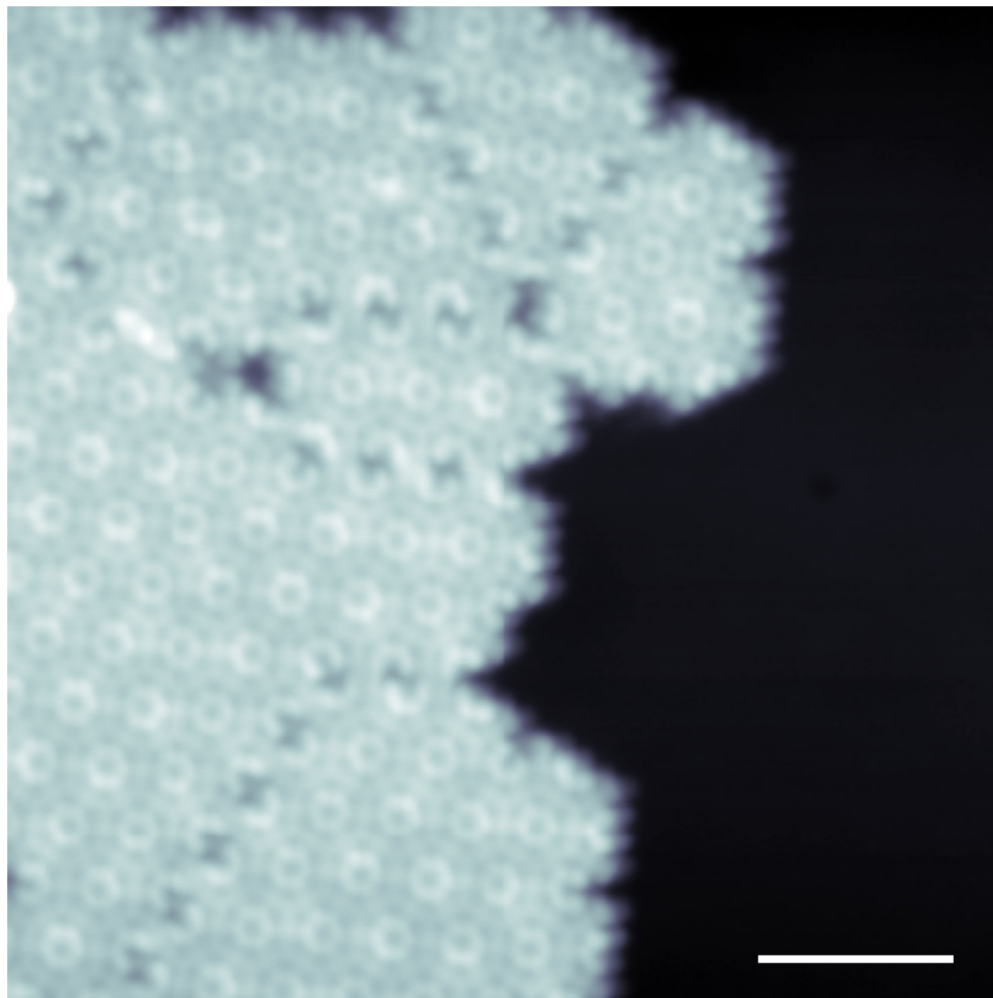


FIG. S2. A large area STM image of DCA_3Co_2 MOF on $\text{G}/\text{Ir}(111)$ surface (dark area) showing various domains of different sizes. The scale bar is 5 nm and the imaging parameters are $V = 1.3$ V and $I = 20$ pA.

Co-N bond lengths

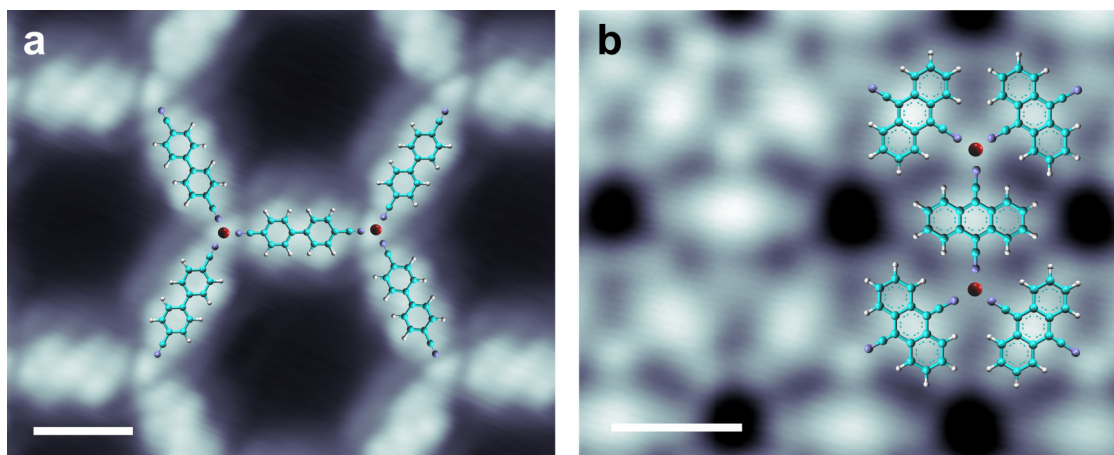


FIG. S3. Scaled molecular structures are overlaid on the STM topography image of **a**, DCBP_3Co_2 and **b**, DCA_3Co_2 MOFs. From here, we extract Co-N bond to be $1.55 \pm 0.5 \text{ \AA}$. Scale bars are 10 \AA .

Assembly of DCA_3Co single complexes on $\text{G}/\text{Ir}(111)$

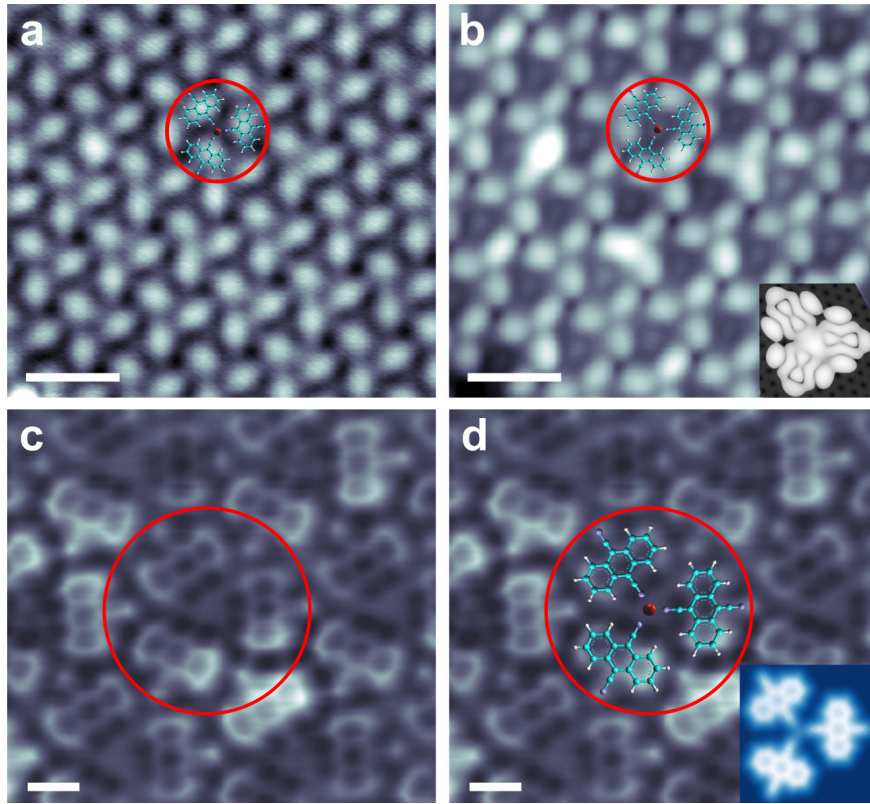


FIG. S4. **a**, A large scale STM image of DCA_3Co single complex assembly recorded at bias, $V = 0.3$ V ($I = 2$ pA) showing the backbone of DCA molecules. The red circle indicates a single complex on the surface. The scale bar is 2 nm. **b**, An STM image of the same area at bias $V = 0.8$ V ($I = 2$ pA) shows LUMO of the DCA molecules and cobalt at the center of the complex. The red circle indicates the same complex indicated in panel a. The inset shows DFT simulated STM image of DCA_3Co complex showing LUMO. **c**, An nc-AFM image of a zoomed-in area shows internal structure of the molecules and their arrangement in the single complex assembly. Again, the red circle indicates a single complex. The cyano groups bonded to cobalt atom are lower than the non-bonded cyano groups. Cobalt atom is not visible at this tip height. **d**, Same as panel c with an overlaid chemical structure of the DCA_3Co single complex. The inset shows a simulated nc-AFM image of the single complex.

Bias dependent STM imaging of DCBP molecule, DCBP₄Co single complex, and DCBP₃Co stripe-phase

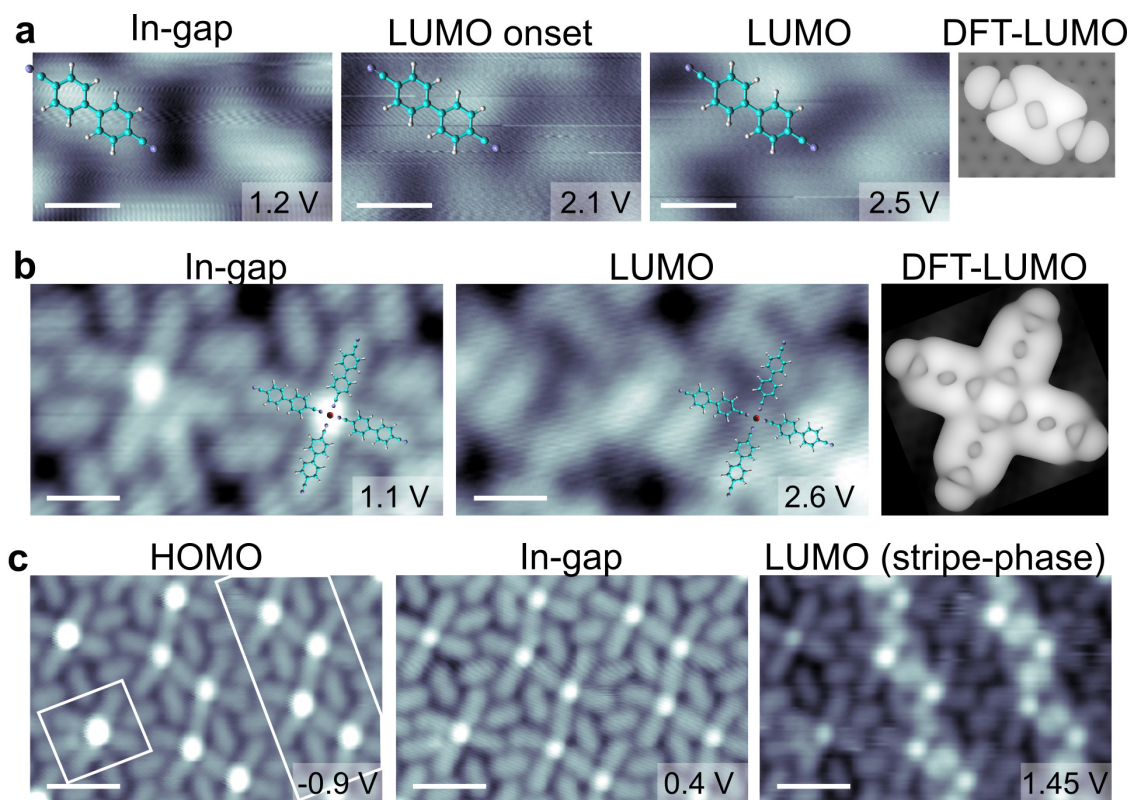


FIG. S5. **a**, Bias dependent STM topography images of DCBP molecules showing backbone (1.2 V), LUMO onset (2.1 V) and LUMO (2.5 V) and DFT simulated STM image showing LUMO. Scale bars are 5 Å. **b**, Bias dependent STM image of DCBP₄Co single complex showing backbone (1.1 V) and LUMO (2.6 V) and DFT simulated STM image depicting LUMO. Scale bars are 1 nm. **c**, Bias dependent STM images of DCBP₄Co single complex and DCBP₃Co stripe showing HOMO (-0.9 V) with a bright cobalt center, in-gap image (0.4 V), and LUMO of DCBP₃Co stripe-phase (1.45 V). Scale bars are 2 nm.

Distance dependent gating on DCBP LUMO due to cobalt atoms

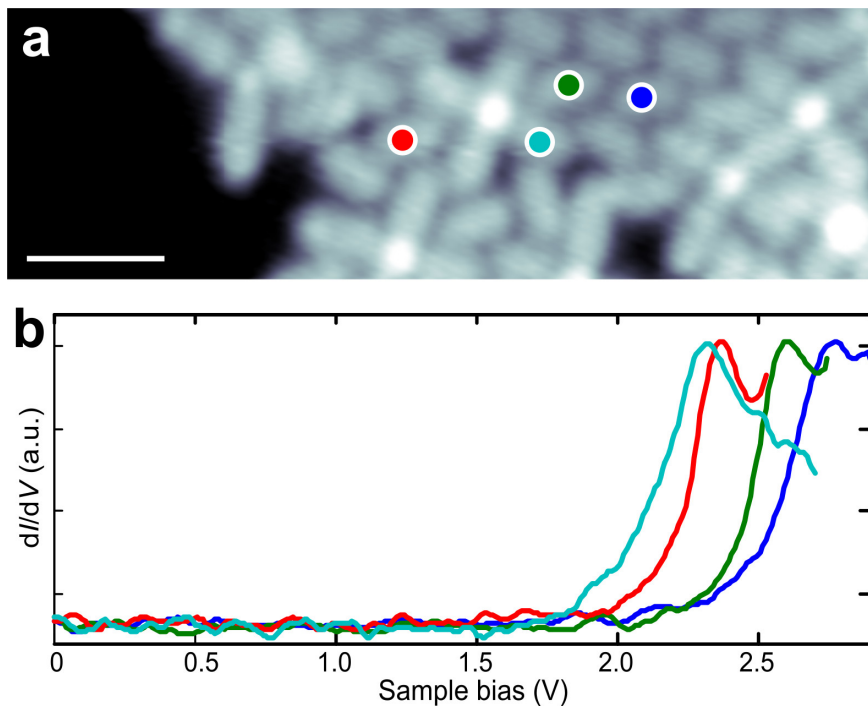


FIG. S6. **a**, STM image of a mixed island of DCBP molecules and DCBP₄Co complexes. The scale bar is 2 nm. Sample bias, $V = 0.77$ V and setpoint, $I = 0.7$ pA. **b**, Gating effect on the DCBP LUMO due to the presence of cobalt metal atoms on the surface. dI/dV spectra are compared for DCBP molecules lying at various distances from the cobalt metal atoms: DCBP molecule far away from the cobalt atoms has LUMO peak at 2.75 V (blue curve) which is very close to the LUMO peak in close-packed molecular assembly. The LUMO peak shifts to 2.60 V (green curve) for a DCBP molecule close to a DCBP₄Co single complex. For another non-bonded DCBP molecule, close to two single complexes, the peak shifts to 2.37 V (red curve). A representative spectrum (cyan curve) on DCBP molecule bonded to a DCBP₄Co single complex has a LUMO peak at 2.30 V.

Assembly of DCA molecules on G/Ir(111)

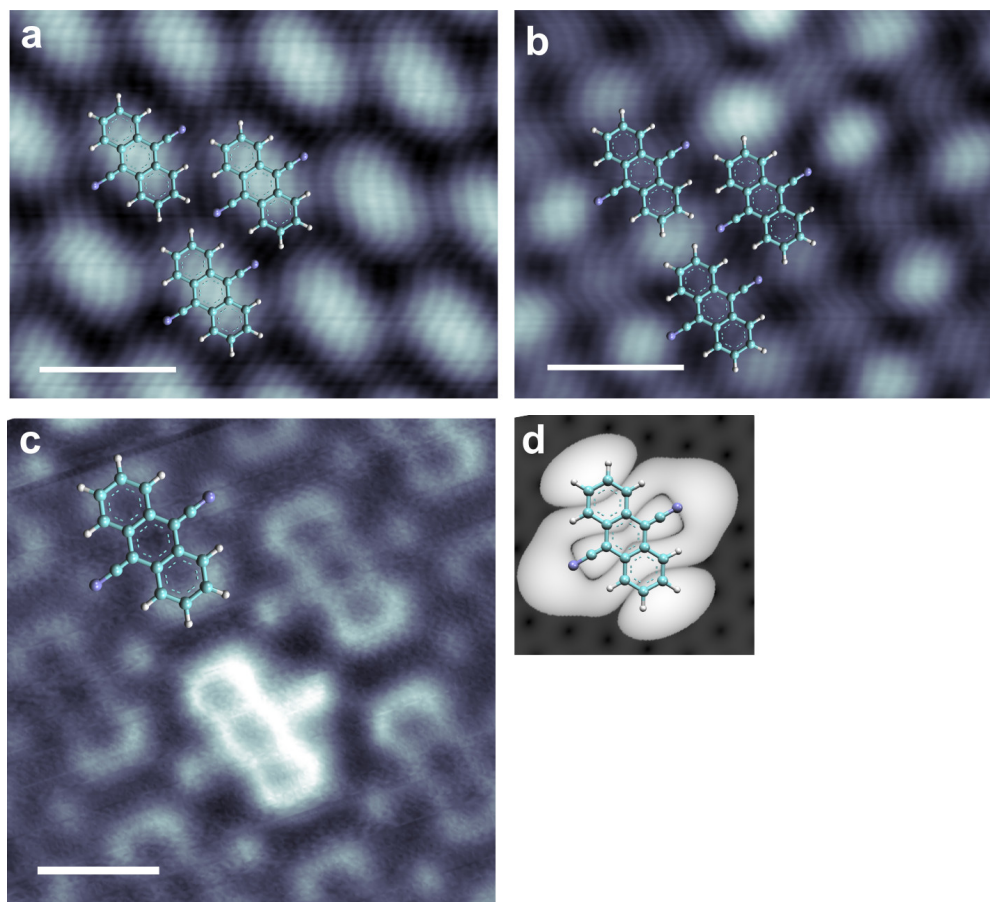


FIG. S7. DCA molecule forms close-packed assembly on G/Ir(111) surface. **a**, STM topography image of DCA molecules at in-gap sample bias $V = 0.4$ V ($I = 1.5$ pA) shows molecular backbone. The scale bar is 1 nm. **b**, STM topography image recorded at 1.6 V ($I = 1.5$ pA) shows LUMO of the DCA. The scale bar is 1 nm. **c**, A zoomed-in nc-AFM image of molecular assembly reveals the structure of the DCA molecules and their arrangement. The scale bar is 5 Å. **d**, DFT simulated STM image of DCA depicting LUMO. Molecular structures are overlaid on each image for the clarity.

dI/dV spectrum on Co in DCBP_3Co_2 MOF

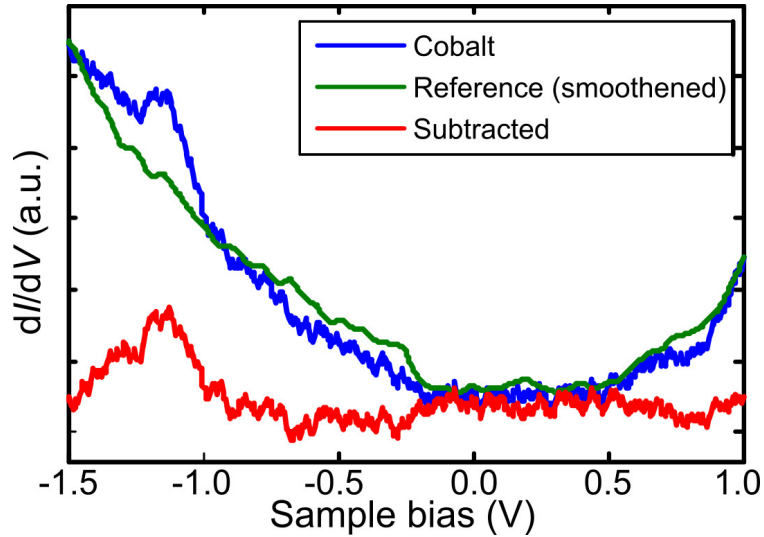


FIG. S8. dI/dV spectrum (blue curve) on Co in DCBP_3Co_2 MOF shows a faint peak at -1.15 V. After subtracting the reference dI/dV spectrum (green curve) recorded on G/Ir(111) surface, we extract the spectrum on Cobalt (red curve).

High spatial-resolution dI/dV spectra on DCA_3Co_2 honeycomb MOF

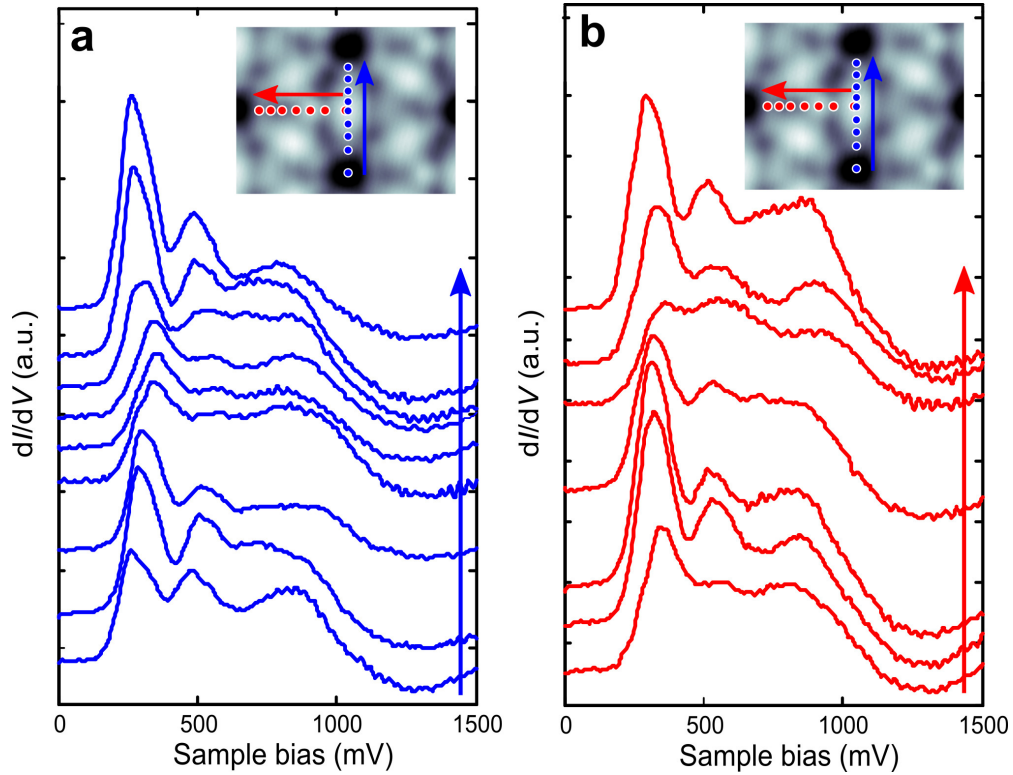


FIG. S9. **a,b** dI/dV point spectra recorded along the backbone of DCA (panel a) and across cobalt atom (panel b) of DCA_3Co_2 MOF as shown in the insets. At the center of the ring of DCA lobes, dI/dV spectra shows peak position at 260 mV which shifts to 290 mV at the position of the lobe which further shifts to 350 mV at the center of the molecule. Across the cobalt atom, the peak position shifts to 320 mV from 350 mV at the center of DCA. Inset imaging parameters $V = 120$ mV and setpoint $I = 33$ pA.

dI/dV spectra on DCA_3Co single complex with DCA_3Co_2 honeycomb MOF

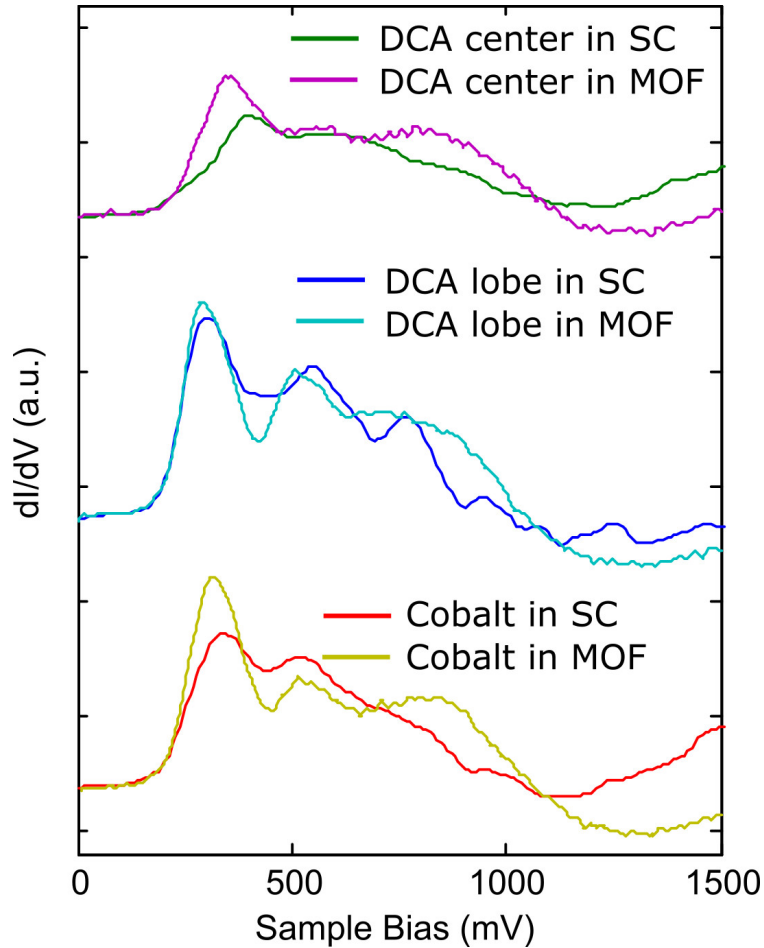


FIG. S10. dI/dV point spectra comparison between DCA_3Co single complex (SC) and DCA_3Co_2 MOF. The spectra at various locations of MOF are displaced vertically w.r.t each other for visualization and the respective SC spectra are vertically displaced too to match MOF spectra. Further, each SC spectrum is shifted towards fermi energy by 470 mV and multiplied by various factors to achieve approximate normalization. Spectra at DCA center, DCA lobe, and cobalt of SC was multiplied by 2.5, 2.7 and 3.1, respectively. Each spectrum recorded on MOF show enhanced NDR effect, due to further decoupling from the substrate as in $DCBP_3Co_2$ MOF. Despite enhanced decoupling, there is at least an excess of states at energies higher than 700 mV.

Band structure and LDOS maps of DCA_3Co_2 MOF for the antiferromagnetic ground state

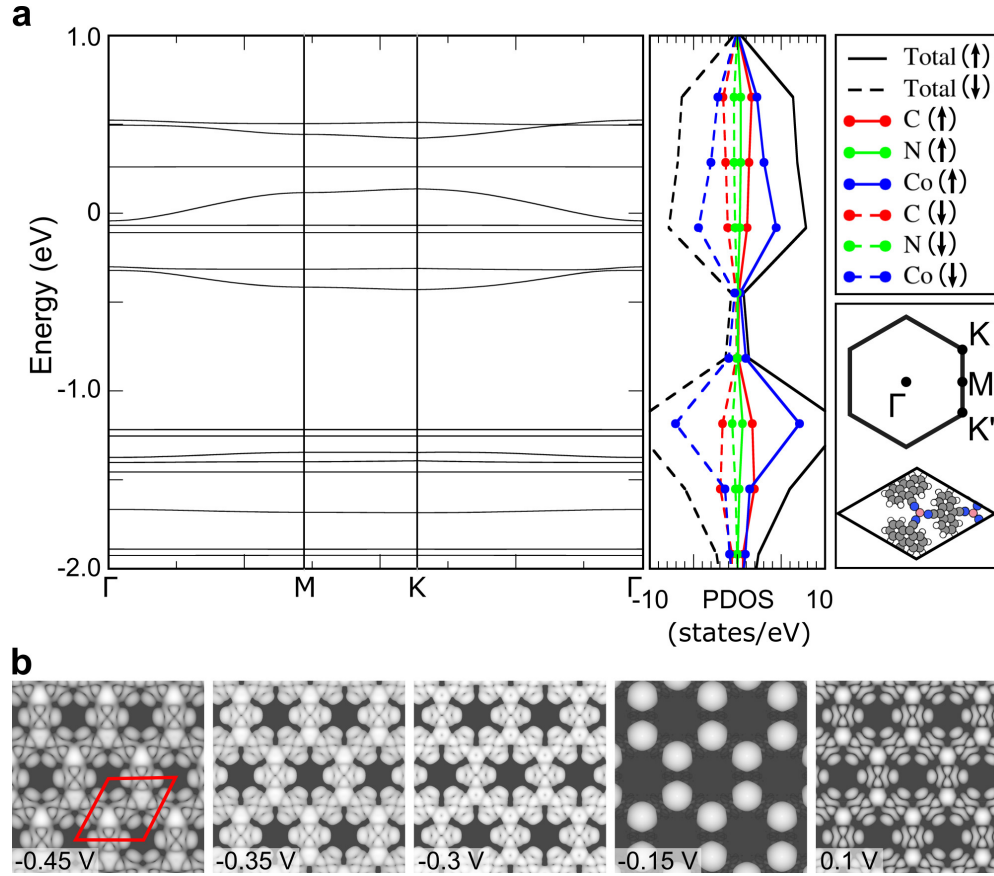


FIG. S11. **a**, Calculated band structure of DCA_3Co_2 MOF for the antiferromagnetic ground state. The band structure shows a number of gaps at Γ -point and smaller gaps at K-point which is inconsistent with the measured dI/dV spectra. While, the top right panels show the partial density of states, the bottom panel shows the unit cell and corresponding Brillouin zone. Presence of a large gap between -0.4 eV and -1.25 eV in the calculated band structure and no observation of states below Fermi energy in the dI/dV spectra until -1.5 V suggests that the energy corresponding to the experimental Fermi level will lie below the flat band at energy -0.3 V. **b**, Simulated LDOS maps for the similar energy range as in measured dI/dV band width shows the LDOS map deviates significantly at -0.15 V from the measured dI/dV maps. The red rhombus represents the unit cell of the structure.

Methods

Sample preparation. The experiment was performed in a Createc low-temperature STM/AFM equipped with a preparation chamber with a base pressure lower than 1×10^{-10} mbar. Ir(111) sample was cleaned by repetitive cycles of sputtering using high energy (2 kV) Ne beam and annealing in oxygen environment at 900 °C followed by flashing to 1300 °C. Graphene was grown by adsorbing ethylene and flashing the sample to 1100 - 1300 °C in a TPG (temperature programmed growth) step followed by a CVD (chemical vapour deposition) step where the Ir(111) substrate at 1100 - 1300 °C is exposed to ethylene gas at 4×10^{-7} mbar pressure for around 60 s. This gives approximately a full monolayer coverage of graphene (G/Ir(111)).

DCBP_xCo_y structures were prepared by sequential deposition of the molecule and cobalt atoms on G/Ir(111) substrate at various temperatures. A submonolayer close-packed assembly of DCBP molecules is achieved by depositing it on G/Ir(111) substrate kept at room temperature using a home build evaporator at 47 °C. Addition of cobalt using a high-temperature effusion cell to the molecular assembly leads to a spontaneous formation of DCBP₄Co single complexes and DCBP₃Co stripe-phase domains depending on the DCBP:Co stoichiometry. To synthesize DCBP₃Co₂ honeycomb MOF, cobalt was further added to the substrate at temperature 60 - 70 °C. After each stage of structure formation, the sample was transferred to the STM and the measurements were performed at 4.5 K.

Similarly, DCA_xCo_y structures were prepared by sequential deposition of the molecule and cobalt atoms on G/Ir(111) substrate at various temperatures. Addition of cobalt to the submonolayer assembly of DCA molecules (evaporation temperature 60 °C) on G/Ir(111) substrate at room-temperature leads to spontaneous formation of assembly of DCA₃Co single complexes. To synthesize DCA₃Co₂ honeycomb MOF, cobalt was further added to the assembly of DCA molecules on G/Ir(111) substrate at ~85 °C. Alternatively, substrate with assembly of DCA₃Co single complexes can be annealed at temperature 80-90 °C for 45 minutes to form small domains of DCA₃Co₂ honeycomb MOF. Prolonged annealing at similar temperature increases the domain size. Also, after each stage of structure formation, the sample was transferred to STM and the measurements were performed at 4.5 K.

STM and AFM experiments. Voltage modulations with amplitude of 10 - 15 mV were used for dI/dV spectra and maps. Mechanically cut Pt/Ir tips were used for all the STM measurements. Non-contact AFM (nc-AFM) measurements were carried out using a qPlus

sensor with resonance frequency $f_0 \sim 30.7$ kHz, a quality factor $Q \sim 10^5$, a spring constant $k \sim 1.8$ kN/m, and an oscillation amplitude of 50 pm. Here, the tips were functionalized by picking up individual CO molecules on a Cu(111) surface as described elsewhere [40, 41]. nc-AFM images were acquired by measuring the frequency shift of the qPlus sensor while scanning over the area in constant height mode. The sample bias during nc-AFM imaging was kept at less than 5 mV. WSxM [42] and Gwyddion [43, 44] software were used to process all STM and nc-AFM images.

Computational All first principles calculations in this work were performed using the periodic plane-wave basis VASP code [45, 46] implementing the spin-polarized density functional theory (DFT). To accurately include van der Waals interactions in this system we used the optB86B+vdW-DF functional, [47–49] selected based on previous work showing that it provides a sufficiently accurate description for all subsystems involved in the measurement. Projected augmented wave (PAW) potentials were used to describe the core electrons, [50] with a kinetic energy cutoff of 550 eV (with `PREC=accurate`). Systematic k -point convergence was checked for all systems, with sampling chosen according to system size. This approach converged the total energy of all the systems to the order of meV. Significantly increased k -point sampling with frozen geometries was used as the basis for the band structure calculations. The properties of the bulk graphite, graphene and the isolated molecular structures were carefully checked within this methodology, and excellent agreement was achieved with experiments where possible. For calculations of the network structures on graphene, system sizes were chosen to minimize lattice mismatch and any remaining strain (less than 1%) was accommodated in the graphene. Note that for calculations of the DCA molecular network on graphene, DFT consistently predicted that the three-fold symmetry seen experimentally would be broken by displacement of the Co closer to two of the nitrogens by about 0.02 Å. Although this is at the limits of our accuracy, we cannot exclude that in reality something else plays a role in maintaining the symmetry, for example the metal substrate. Since asymmetric structures were never observed experimentally, we constrained the system to be three-fold symmetric. On graphene, the calculations suggest displacement of Co towards the surface (larger than for DCBP₃Co₂), which is not really seen in the experiment. Symmetric and asymmetric systems had minor differences in their band structures, especially compared to those between antiferromagnetic and ferromagnetic cases. As a further check, we also performed calculations on a DCA₃Mn₂ framework using

the same approach, and found very similar results to those published previously [7].

STM images were calculated using the HIVE package [51]. For calculated AFM images we used our implementation of the model developed by Hapala *et al.* [52]. The molecular structure was taken from DFT simulations and the electrostatic potential was extracted from the Hartree potential [52, 53]. The mechanical AFM model relies on empirical Lennard-Jones parameters, which were taken from the CHARMM force field [54]. The best agreement with experiment was found with a tip lateral spring constant of about 0.5 N/m, similar to values reported in previous studies [55]. All other parameters are the same as intended by Hapala *et al.*, and the simulated AFM scan is performed at a resolution of 5 pm (in all directions), with a force tolerance criterion of $4 \times 10^{-6} \text{ eV\AA}^{-1}$. The 3D force field is subsequently converted into a frequency shift image [56], using the experimental parameters.